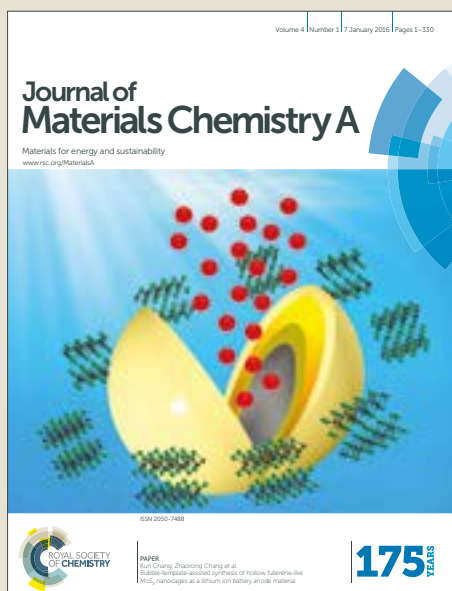


Journal of Materials Chemistry A

Accepted Manuscript



This article can be cited before page numbers have been issued, to do this please use: T. Li, Y. Lu, S. Zhao, Z. Gao and Y. Song, *J. Mater. Chem. A*, 2018, DOI: 10.1039/C7TA11171A.



This is an Accepted Manuscript, which has been through the Royal Society of Chemistry peer review process and has been accepted for publication.

Accepted Manuscripts are published online shortly after acceptance, before technical editing, formatting and proof reading. Using this free service, authors can make their results available to the community, in citable form, before we publish the edited article. We will replace this Accepted Manuscript with the edited and formatted Advance Article as soon as it is available.

You can find more information about Accepted Manuscripts in the [author guidelines](#).

Please note that technical editing may introduce minor changes to the text and/or graphics, which may alter content. The journal's standard [Terms & Conditions](#) and the ethical guidelines, outlined in our [author and reviewer resource centre](#), still apply. In no event shall the Royal Society of Chemistry be held responsible for any errors or omissions in this Accepted Manuscript or any consequences arising from the use of any information it contains.

Graphical abstract



Carbon-encapsulated Co₃O₄-doped Co/CoFe bifunctional catalyst prepared by annealing LDH acts as a highly efficient air cathode in rechargeable Zn-air battery.



Journal Name

ARTICLE

Co₃O₄-doped Co/CoFe Nanoparticles Encapsulated in Carbon Shell as Bifunctional Electrocatalyst for Rechargeable Zn–Air Batteries

Tongtong Li,^a Yongxin Lu,^a Shuaishuai Zhao,^a Zhi-Da Gao^{*a} and Yan-Yan Song ^{*a}

Received 00th January 20xx,
Accepted 00th January 20xx

DOI: 10.1039/x0xx00000x

www.rsc.org/

The development of catalysts based on non-precious metals and able to catalyze both the oxygen reduction and oxygen evolution reactions (ORR/OER) is the key element to promote the practical application of rechargeable metal-air batteries. Here we report a novel concept that layered double hydroxides (LDH) can be used as a precursor to form bimetal and their oxides simultaneously. Co₃O₄-doped Co/CoFe nanoparticles integrated with graphitic shells are derived from the thermal decomposition of a CoFe LDH bonded with urea as carbon precursor. The composite material shows a surprisingly high bifunctional (ORR/OER) catalytic activity. The realized core-shell structure synergistically promotes the ORR performance while cobalt oxide doped on the metal surface boosts the OER performance. In addition, the carbon shell ensures the high electrical conductivity and effectively impedes the aggregation and the further oxidation of Co/CoFe nanoparticles. When integrating the catalyst in a rechargeable Zn-air battery, the battery performance shows a higher discharging potential and cycling stability (over 65 h cycling test) and a lower charging plateau compared with a Zn-air battery based on the Pt/C and RuO₂ catalyst mixture. This work demonstrates a new efficient air cathode material which could be practically applied in rechargeable metal–air batteries or other fuel cells.

Introduction

Zinc-air batteries (ZABs), are within the most promising energy conversion technology which displays characteristics of both a fuel cell and a battery; ZABs have been applied in electric vehicles and small electronic devices due to the high energy density, discharge stability, low cost and safe operation.^{1,2} The oxygen reduction reaction (ORR) and the oxygen evolution reaction (OER) are the two key kinetic processes occurring during the ZAB discharge and charge.³⁻⁵ Since these two reactions are slow, to develop efficient and robust catalysts for ZABs is of critical importance especially for the rechargeable air cathode. Noble metal-based catalyst materials such as Pt/C and RuO₂ exhibit excellent activity to reduce the overpotential of the ORR and the OER, respectively. However, these catalysts are limited by their high cost and low abundance and that is why enormous efforts have been devoted to investigate alternative earth-abundant high performance catalysts.⁶⁻¹⁰ Recently, transition metal combined with carbon nanomaterials (i.e., carbon nanotubes, graphene, graphitic arrays, etc.) have been widely applied to promote the ORR.¹¹⁻¹³ For the OER, efficient electrocatalysts have been reported based on Co₄N, CoSe₂ and Co₃O₄, supported on carbon

materials.¹⁴⁻¹⁶ The transition metal cations in the compounds not only boost the electrostatic affinity with OH⁻ ions but also enhance the electrophilicity of the adsorbed oxygen (O_{ad}) during water splitting.^{17, 18} Moreover, bifunctional oxygen electrocatalysts based on transition metal and their derivatives have attracted considerable attention in recent years.¹⁹⁻²¹

Layered double hydroxides (LDHs) are a unique class of typical two-dimensional (2D) layered materials. The general structural formula of LDHs is [M^{II}_{1-x}M^{III}_x(OH)₂]^{x+}[A_{x/n}]ⁿ⁻·yH₂O. In this structure, some of bivalent metal cations (M^{II}: Mg²⁺, Co²⁺, Ni²⁺, Ca²⁺, Zn²⁺, etc.) are replaced by trivalent metal cations (M^{III}: Al³⁺, Fe³⁺, Cr³⁺, Ga³⁺, In³⁺, etc.) to give positively charged layers; interlayer anions (A: CO₃²⁻, NO₃²⁻, SO₄²⁻, Cl⁻, etc.) and water molecules stabilize the structure by electrostatic interactions as well as hydrogen bonds.^{22, 23} Due to their tunable compositions and ordered nanostructure, LDHs have been widely applied as catalysts, adsorbents, optical and magnetic materials and the components of drug delivery.²³⁻²⁶ Researchers have found several classes of LDHs have excellent electrocatalytic activity toward oxygen evolution reaction.^{27, 28} But few of them aimed to construct the bifunctional catalysts based on LDH for both OER and ORR. Till very recently, Zhang and coworkers reported Co₃FeS_{1.5}(OH)₆ hydroxysulfides as bifunctional OER/ORR electrocatalyst for Zn-air battery by treating graphene-supported CoFe hydroxide with a very high-concentration S²⁻ solution for 24 h.²⁹ And Zhang attached NiFe LDH nanoparticles to Co,N-codoped carbon nanoframes to achieve a good bifunctional activity.³⁰ Thus, finding an facile and effective approach to develop high-performance

^a College of Sciences, Northeastern University, Shenyang 110004, China. E-mail: gaozd@mail.neu.edu.cn; yysong@mail.neu.edu.cn

† Electronic Supplementary Information (ESI) available: additional PXRD, SEM, TEM, AFM, XPS, BET and CV tests. See DOI: 10.1039/x0xx00000x

ARTICLE

Journal Name

bifunctional catalyst based on LDH is important for rechargeable metal-air battery.

In this work, we demonstrate one-step annealing method to synthesize carbon-encapsulated Co_3O_4 -doped Co/CoFe nanostructures (denoted as 3C-900). The composite is fabricated from homogeneously dispersed Co and Fe ions in a CoFe LDH acting as the metal source, urea as the carbon precursor and PEG-PPG-PEG (Pluronic P123) as the surfactant. The resulting Co/CoFe nanoparticles are encapsulated by a graphitic carbon shell and doped by a small fraction of cobalt oxide generated from the decomposition of the LDH. The as-made 3C-900 shows outstanding catalytic performance for both ORR and OER reactions. Using the optimized catalyst as the air cathode, the as-prepared ZABs show excellent rechargeable performance and long cycling life, overwhelming ZABs based on the Pt/C and RuO_2 mixed catalysts.

Results and discussion

Characterization

The X-ray diffraction (XRD) pattern of the as-synthesized CoFe LDH is shown in Fig. S1; the peaks are ascribed to the

hydrotalcite-like materials, $\text{Co}_{5.84}\text{Fe}_{2.16}(\text{OH})_{16}(\text{CO}_3)_{1.08}\cdot 0.32\text{H}_2\text{O}$ (#JCPDS 050-0235). Scanning electron microscopy (SEM) and transmission electron microscopy (TEM) images (Fig. S2) confirmed the sheet-like structure of LDH with a size of several hundreds of nanometers. High-resolution TEM (HR-TEM, Fig. S2c) image shows that the interplanar distance is 2.44 Å, corresponding to the (104) lattice planes spacing in CoFe LDH. The (101) and (113) planes of LDH can be identified from the corresponding selected area electron diffraction (SAED) patterns on TEM images (Fig. S2d). A typical stacking structure of several individual LDH nanosheets is evident from atomic force microscopy images (AFM, Fig. S3). Using the homogeneously dispersed Co and Fe ions from the CoFe LDH as the metal source, urea attached to LDH as the carbon precursor, and P123 as the surfactant, a three-dimensional (3D) coral-like nanostructure is obtained after the annealing in a N_2 atmosphere at 900 °C (Fig. S4). The TEM image in Fig. 1a shows that the coralline clusters are composed of several nanoparticles (of about 25 nm) embedded in carbon shells. The HR-TEM image in Fig. 1b further confirms the core@shell structure of the as-made 3C-900 catalyst. The graphitic carbon wrapping is characterized by the (002) plane showing an

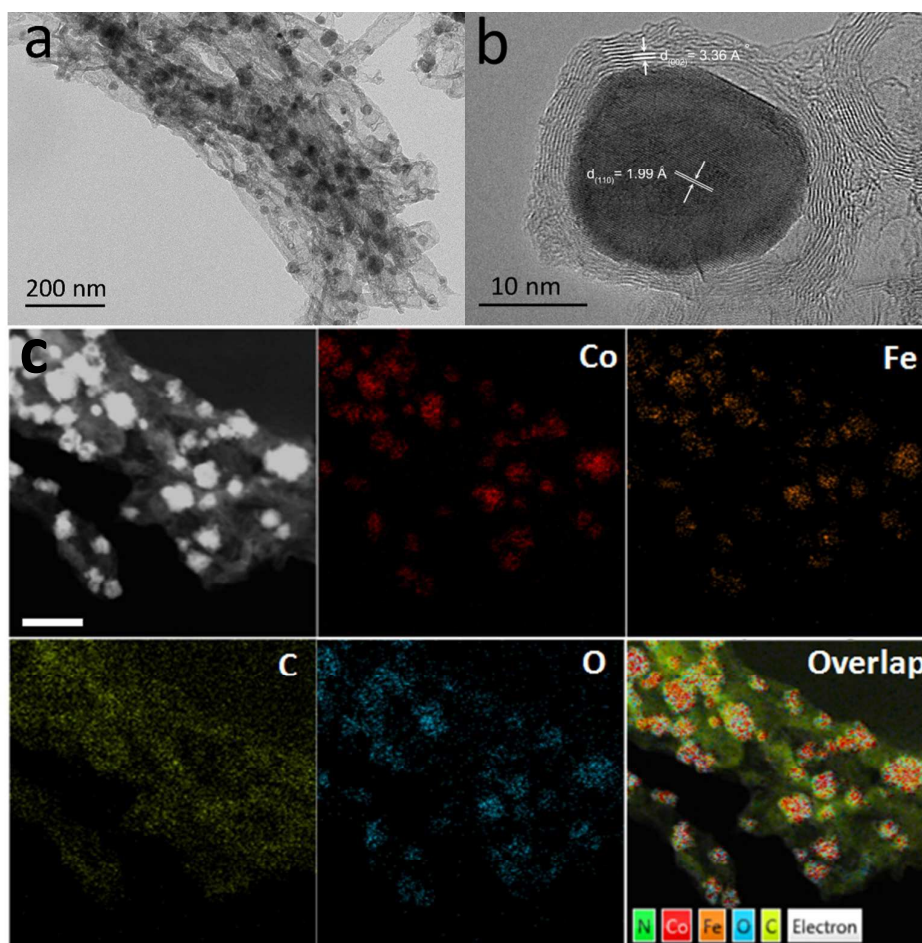


Figure 1. (a) TEM-image, (b) HR-TEM image of the sample 3C-900. (c) STEM-image and corresponding EDX mappings of Co, Fe, C, and O elements in the sample 3C-900. The scale bar is 100 nm.

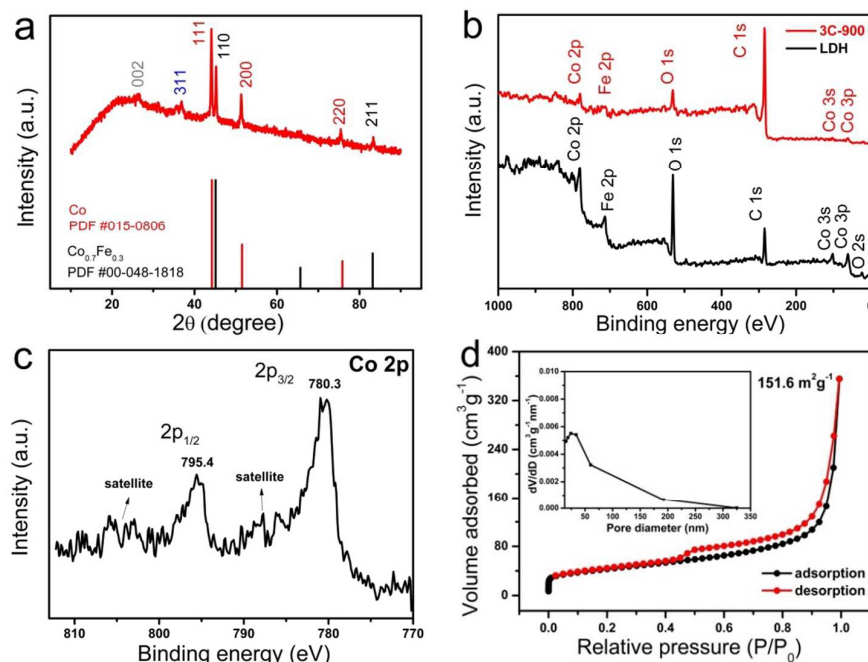


Figure 2. (a) XRD pattern sample from 3C-900. (b) XPS survey spectrum of 3C-900 and of the CoFe LDH. (c) High-resolution XPS spectra of Co 2p from 3C-900. (d) N₂ adsorption-desorption isotherms of 3C-900. The inset in (d) shows the corresponding pore size distribution.

interlayer spacing of 0.336 nm, while the inner core exhibits the interlayer spacing of 0.199 and 0.206 nm (Fig. S4) corresponding to the (110) plane of the CoFe alloy and the (111) plane of the metallic cobalt, respectively. The high-angle annular dark-field scanning TEM (HAADF-STEM) image and the corresponding EDX elemental mapping (Fig. 1c) show that both Co and Fe elements are homogeneously distributed in the nanoparticles and that O species are uniformly distributed on the particles outline, suggesting the presence of oxides. In addition, N signal distribution is consistent with C signal indicating that the carbon shells are slightly N-doped (Fig. S5).

The coexistence of the metallic cobalt, the CoFe alloy and their oxides is further confirmed by XRD and X-ray photoelectron spectroscopy (XPS) analyses. The XRD pattern in Fig. 2a shows a broad diffraction peak at 20°–30°, indicating the presence of the amorphous carbon. The peak at 26.2° is ascribed to (002) plane of graphitic carbon, which is formed by the thermal decomposition of urea at 900 °C. The sharp diffraction peaks at 44.2°, 51.5°, and 75.9° are indexed to (111), (200), and (220) crystal planes of metallic cobalt phases (PDF No. 015-0806), while the peaks at 45.1°, 65.7°, and 83.2° corresponds to (110), (200), and (211) crystal facets of the Co_{0.7}Fe_{0.3} alloy (PDF No. 00-048-1818). The presence of cobalt oxide is proved by the peak at 36.9° corresponding to (311) spacing in Co₃O₄ (PDF No. 01-074-1656). The XPS survey spectra of LDH and 3C-900 indicate the presence of C, O, Co, N and Fe species without any other impurity elements (Fig. 2b). The atomic percentages of C, O, Co, Fe and N in 3C-900 are estimated to be 89.7%, 6.9%, 1.3%, 1.0% and 1.1%, respectively. The Co 2p high-resolution spectrum (Fig. 2c) obtained on 3C-900 showing the Co 2p_{3/2} and Co 2p_{1/2} doublet components are centered at 780.3 and 795.4 eV binding

energy as compared to those of pure metallic Co at 778.0 and 793.0 eV, indicating the presence of oxide species in the composite.^{31, 32} This is further confirmed by the multiplet splitting of the spin doublet and the obvious shake-up satellite peaks at 787.1 and 805.0 eV.^{33, 34} The N₂ adsorption-desorption curves obtained in the sample 3C-900 are shown in Fig. 2d: a typical type-IV isotherm with an obvious hysteresis is obtained, indicating the presence of mesopores. The corresponding Brunauer–Emmett–Teller (BET) surface area is 151.6 m²g⁻¹. The Barrett–Joyner–Halenda (BJH) pore size distribution obtained from the N₂ desorption data confirm the presence of mesopores with pore diameters in the range between 10 and 50 nm in the coral-like structure.

Electrocatalytic activities for the ORR and OER

The cyclic voltammogram (CV) and liner scan voltammogram (LSV) have been executed to evaluate the electroactivity of the catalyst. For comparison, a CoFe reference (obtained without using the LDH template) and other references samples have been prepared by the same reaction steps. The oxygen reduction peaks are observed from the O₂-saturated KOH solution for all the catalysts while absent in the N₂-saturated KOH solution (Fig. S6). It can be noticed that the ORR activity of the catalysts is affected by the presence of the LDH template, the carbon precursor, the surfactant (Fig. S6), and the annealing temperature (in Fig. S7, the samples prepared at 600, 700, and 800 °C are denoted as 3C-600, 3C-700, and 3C-800). Owing to better graphitization degree, the 3C-900 exhibits a higher ORR activity that a pronounced cathodic peak appears at more positive potential compared with other references samples. The ORR catalytic activity of 3C-900 is

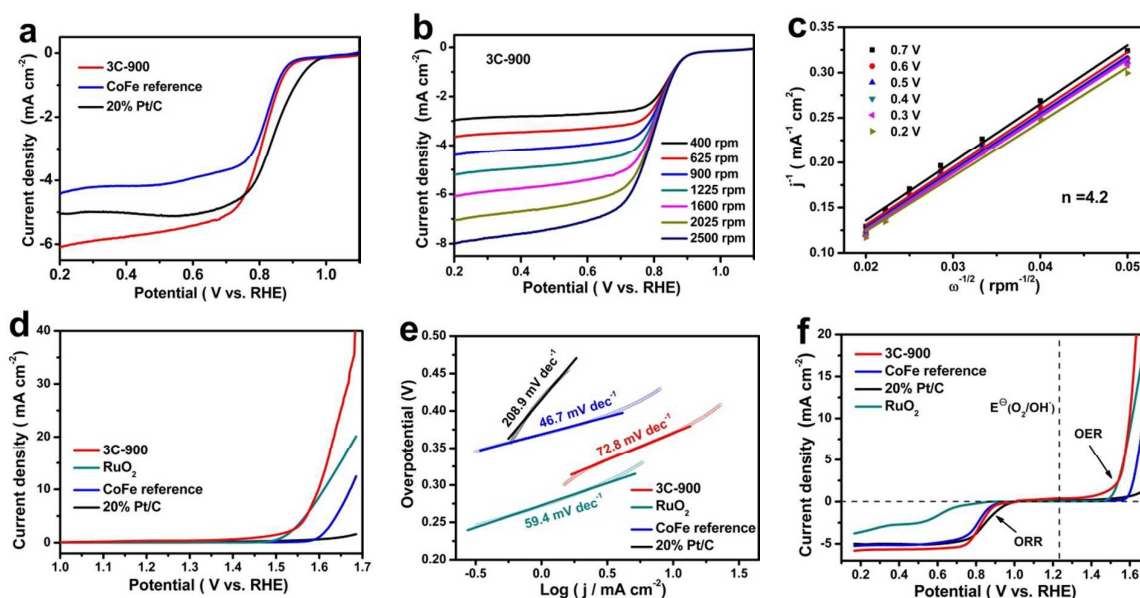


Figure 3. (a) ORR polarization curves of the 3C-900, CoFe reference, and the 20% Pt/C catalyst in O_2 -saturated 0.1 M KOH at 1600 rpm. (b) ORR polarization curves of 3C-900 at different rotation speeds. (c) Corresponding K-L plots at different potentials. (d) OER polarization curves of the 3C-900, CoFe reference, RuO_2 and 20% Pt/C catalyst in O_2 -saturated 0.1 M KOH at 1600 rpm. (e) Tafel slopes derived from (d). (f) The overall polarization curves of the ORR and OER for different catalysts (Rotation rate: 1600 rpm; Electrolyte in 0.1 M KOH; Sweep rate: 5 mV s^{-1}).

further investigated using a rotating disk electrode (RDE). Fig. 3a show the LSV curves of the 3C-900, the Pt/C and the reference CoFe samples measured with the RDE. The 3C-900 shows a prominent electrocatalytic performance characterized by a more positive onset potential and half-wave potential respect to the CoFe reference. Although the onset potential in the 3C-900 is slightly lower than in the commercial Pt/C, its ORR activity outperforms most of the previously reported non-precious metal-based catalysts.³⁵⁻³⁷ The ORR kinetics was further analyzed by the polarization plots at various rotating speeds (Fig. 3b). The electron transfer numbers per O_2 (n) for the ORR are calculated by the corresponding Koutecky–Levich ($K-L$) plots (j^{-1} vs $\omega^{-1/2}$) according to the ($K-L$) equation (Fig. 3c, Fig. S8 and Fig. S9). The n values for 3C-900, CoFe reference, 3C-600, 3C-700 and 3C-800 result 4.1, 4.1, 4.0, 4.0 and 3.9. The small difference also respect to the Pt/C catalysts ($n=4.1$) in the voltage range between 0.2 and 0.7 V implies a common four-electron pathway for the ORR. The number obtained is slightly over 4 because of the probable deviation between theoretical value (D_o , v , C_o) in the Koutecky–Levich equation and experimental value. In contrast, the electron transfer numbers of other reference samples (Fig. S10) are much lower, suggesting a combined two-electron and four-electron ORR pathway. Moreover, the ORR efficiency measured by the rotating ring-disk electrode (RRDE) shows a similar trend (Fig. S11). The HO_2^- yield in sample 3C-900 is about 20% at each potential with n ranging from 3.54 to 3.63. The value is slightly higher than that from CoFe reference (HO_2^- : 21.6%–28.4%; n : 3.42–3.57) and similar to that of the 20% Pt/C (HO_2^- : 2.9%–13.1%; n : 3.73–3.94). Chronoamperometric curves in Fig. S12 show that the 3C-900 maintains 93% of its original ORR current density after 15000 s of continuous operation at 0.75 V, whereas the Pt/C catalyst suffers a significant loss with only

78% retention. After adding 1 M methanol to the electrolyte, the current density of Pt/C changes significantly due to the methanol oxidation reaction, while the 3C-900 doesn't show any noticeable current decrease. These results indicate that the 3C-900 catalyst displays long-term stability, strong methanol tolerance and high selectivity for the ORR.

The OER properties of 3C-900 were also assessed by the LSV test, which is performed in O_2 -saturated 0.1 M KOH with a RDE at 1600 rpm to remove the generated O_2 bubbles. As shown in Fig. 3d–e, the 3C-900 catalyst results in earlier onset potential compared to commercial RuO_2 and a Tafel slope of 72.8 mV dec^{-1} . Impressively, the 3C-900 catalyst achieves the current density of 10 mA cm^{-2} at an overpotential smaller than what observed with the RuO_2 catalyst. The earlier onset potential and much higher current density in a wide potentials range indicate a higher OER activity of the 3C-900 catalyst (Fig. 3d, Fig. S13). Chronoamperometry was performed to assess the stability of the catalysts. Figure S14 shows that the 3C-900 and the commercial RuO_2 catalysts undergo a similar activity loss under continuous OER operations for 16000 s at 1.60 V. This obvious degradation mainly originates from the peeling of the catalyst coating from the electrode surface during the evolution of O_2 bubbles.^{16, 38} In addition, the corrosion of the carbon support under the relatively high potential also influences the catalyst stability.³⁹⁻⁴¹ In Fig. 3f, the bifunctional activities of the catalysts are evaluated from the difference between the potential measured at the OER current density of 10 mA cm^{-2} and ORR current density of -3 mA cm^{-2} ($\Delta E = E_{j10} - E_{j-3}$). The ΔE value (0.78 V) obtained for the 3C-900 catalyst is considerably smaller than the one from CoFe (0.88 V) or noble metals (e.g., RuO_2 : 1.3 V; Pt/C: $>0.94\text{ V}$) or many non-precious metal-based bifunctional catalysts reported before (Table S1); this further confirms the outstanding catalytic activity of the

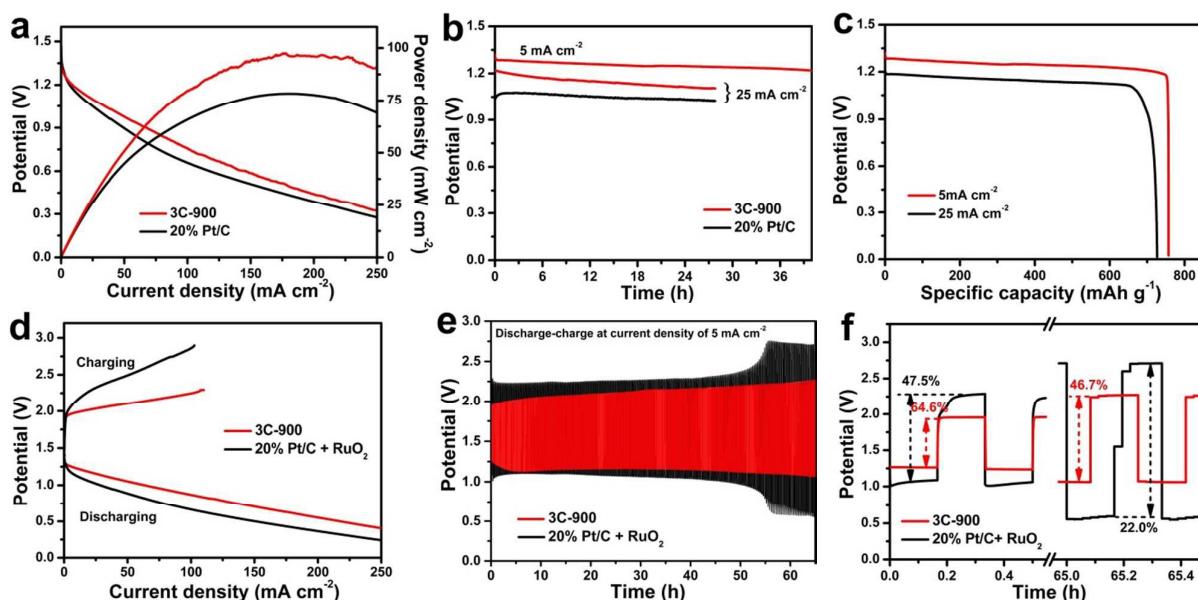


Figure 4. (a) Polarization and power density curves of primary Zn-air batteries using 3C-900 and 20% Pt/C as ORR catalyst of the air cathode, respectively. (b) Discharge curves of the primary Zn-air batteries using various ORR catalysts at different current densities (5 and 25 mA cm⁻²). (c) Specific capacities of the Zn-air batteries using 3C-900 as ORR catalyst, which is normalized to the mass of the consumed Zn. (d) Charge and discharge polarization curves of the rechargeable Zn-air batteries. (e, f) Charge and discharge cycling curves of the rechargeable Zn-air batteries at a current density of 5 mA cm⁻².

3C-900 towards both the ORR and the OER.

The unique core-shell structure of the 3C-900 combines the bimetal nanoparticles with the conductive graphitic carbon coating, which effectively accelerate the electron and mass transfer during the catalytic reaction. The nitrogen-doped carbon shell not only offers additional active sites for the ORR, but also impedes the metal cores from further oxidation and accumulation, thus enhancing the ORR and OER stability. The higher OER performance of the 3C-900 respect to the CoFe reference is attributed to the minor Co₃O₄ content derived from the decomposition of LDH. The formation of the OOH species is an important step in OER process (see the ESI), the presence of cobalt cations can both (i) attract OH⁻ ions via electrostatic affinity and (ii) lower the thermodynamic barrier to form intermediate OOH_{ad} states by enhancing the electrophilicity of the OH_{ad}.^{17, 42-44} Compared with the layered double hydroxides, the use of nitrate as the metal source cannot provide for sufficient oxygen source to form the metal oxides in the reference CoFe sample.

Primary Zn-air batteries

The primary Zn-air battery was first constructed to evaluate the ORR performance of the 3C-900 catalyst. The open-circuit potential (OCP) of the battery is ~ 1.43 V (Fig. S15). As shown in Fig. 4a, the 3C-900 allows for a high current density of 180 mA cm⁻² and a peak power density of ~ 97 mW cm⁻², which is better than what obtained with the Pt/C catalyst (180 mA cm⁻² and 78 mW cm⁻²). After a long-term galvanostatic discharge at 5 mA cm⁻² for ~42 h and 25 mA cm⁻² for ~28 h, no obvious voltage drop is observed, indicating the good catalytic stability

for the ORR (Fig. 4b). In addition, the battery shows a high voltage plateau of ~1.2 V at the current density of 25 mA cm⁻², slightly outperforming the battery made with 20% Pt/C (~1.1 V). The specific capacity of the battery normalized to the mass of consumed Zn at the current density of 5 and 25 mA cm⁻² is 757 and 727 mAh g⁻¹, corresponding to energy densities of 942 and 819 Wh kg⁻¹, respectively (Fig. 4c). This result is better than recently reported ZABs.^{45, 46} The specific capacity of the 3C-900 at 5 mA cm⁻² reaches ~90% of the theoretical capacity (~824 mAh g⁻¹). Two Zn-air batteries connected in series can generate an OCP of ~ 2.9 V which is sufficient to illuminate three light-emitting diodes (LEDs) or a ~ 0.2 W bulb (Fig. S15 and S16).

Rechargeable Zn-air batteries

The 3C-900 bifunctional catalyst is further investigated in a two-electrode rechargeable ZAB. To facilitate the reversible Zn electrochemical reactions at the anode, 0.2 M zinc chloride is added into the 6 M KOH electrolyte. The mixture of Pt/C and RuO₂ is also tested as the air cathode for comparison. The lower charge-discharge voltage gap of the 3C-900 catalyst resulting from the discharge and charge polarization curves (Fig. 4d), indicate the excellent rechargeability of our Zn-air battery. This property is confirmed by the 180 discharge/charge cycles test lasting for 65 h at a current density of 5 mA cm⁻², as shown in Fig. 4e. Compared with the Pt/C - RuO₂ catalyst, the 3C-900 based ZAB exhibits a lower charging potential and a higher discharging voltage plateau, which demonstrate the higher catalytic activity towards both the OER and the ORR. After the prolonged cycling test, a

ARTICLE

Journal Name

considerable loss is observed in the ZAB electrocatalytic activity due to the unavoidable deactivation of the catalyst following the strong oxidation and reduction occurring during the battery cycling.^{3, 4, 47} Nevertheless, the 3C-900 based ZAB performance results to overcome the one from the Pt/C - RuO₂ ZAB (Fig. 4f). Clearly, the voltaic efficiency, corresponding to the voltage at the end of the discharge divided by the voltage at the end of the charge of 3C-900 decreases by 64.6% at the 1st cycle till 46.7% at the 180th cycle, while with the Pt/C - RuO₂ mixture at the 180th cycle, the voltaic efficiency decreases dramatically to 22%.

Conclusions

In summary, we prepared a carbon-encapsulated Co₃O₄-doped Co/CoFe nanostructure as a novel bifunctional catalyst for rechargeable Zn-air batteries. The one-step annealing strategy utilizing CoFe LDH as a precursor of both metal and metal oxide is simple and effective. Owing to the synergistic effect of graphitic-carbon shell and the small fraction of Co oxide in Co/CoFe core, the 3C-900 electrocatalyst exhibited outstanding bifunctional catalytic activity toward both the ORR and the OER. The Zn-air batteries based using the 3C-900 as the air cathode showed a high specific capacities of 757 and 727 mA h g⁻¹ (corresponding to the energy densities of 942 and 819 Wh kg⁻¹) at the current densities of 5 and 25 mA cm⁻², respectively. Compared to a ZAB based by noble metal catalyst, the 3C-900 rechargeable ZAB showed a smaller voltage polarization and a better stability during its continuous cycling operation over 65 h. We believe this work will offer an inspiring route to prepare efficient, stable, cost-effective and earth-abundant bifunctional ORR/OER catalysts for rechargeable Zn-air batteries or other electrocatalytic applications.

Experimental

Materials

Cobalt nitrate hexahydrate (Co(NO₃)₂·6H₂O), ferric nitrate nonahydrate (Fe(NO₃)₃·9H₂O), sodium hydroxide (NaOH), sodium carbonate (Na₂CO₃), potassium hydroxide (KOH), zinc chloride (ZnCl₂), urea and ethanol were purchased from Sinopharm Chemical Reagent Co., Ltd. PEG-PPG-PEG (Pluronic P123, average M_n ~5800) and Nafion (5.0 wt%) were purchased from Sigma-Aldrich. Pt/C (20 wt% Pt on carbon) was purchased from Shanghai Macklin Biochemical Co., Ltd. RuO₂ was purchased from Aladdin Co., Ltd. Carbon cloth (CC) was purchased from CeTech Co., Ltd. All chemicals were used as received without any further purification. All aqueous solutions were prepared with deionized (DI) water.

Synthesis of CoFe LDH

The CoFe LDH precursors were prepared by the separate nucleation and aging steps (SNAS) according to ref. [48] with some revision. Typically, Co(NO₃)₂·6H₂O and Fe(NO₃)₃·9H₂O was dissolved in deionized water with Co/Fe molar ratio of 3.0

to give solution A. The aqueous solution containing NaOH and Na₂CO₃ with the concentration ratio of 2.5 formed the solution B. Then, equal volumes of solution A and B were mixed under vigorous stirring and the resulting slurry was aged at 80 °C for 48 h followed by washing thoroughly with water and ethanol by centrifugation. The LDH was finally dried at 60 °C.

Synthesis of electrocatalyst

To prepare electrocatalyst, 0.2 g LDH, 1.44 g urea and 0.75 g P123 were dissolved into 15 mL deionized water and the mixture was stirred and evaporated at 80 °C. The obtained solid samples were placed in the center of the tube furnace (Lindberg/Blue M, TF55035KC-1) and heated at 500 °C for 2 h under a steady flow of N₂. Then the temperature was further raised to 600, 700, 800, 900 °C, respectively, and maintained for 2 h in N₂ atmosphere to get 3C-600, 3C-700, 3C-800, and 3C-900. Similarly with 3C-900, the CoFe reference were obtained by replacing the LDH with the solution of Co(NO₃)₂·6H₂O and Fe(NO₃)₃·9H₂O as the metal source. The other control groups were also prepared through the same procedure of 3C-900 just without LDH, P123, and urea, respectively.

Materials characterization

The catalysts morphology was characterized by using a field-emission scanning electron microscopy (Hitachi FE-SEM S4800) and transmission electron microscopy (TEM, JEOL 2000). Powder X-ray diffraction (XRD) patterns were collected using an X'Pert Pro MPD diffractometer (PANalytical) with Cu K α radiation. X-ray photoelectron spectra (XPS) were obtained with a Perkin-Elmer Physical Electronics 5600 spectrometer. The surface roughness was studied by the atomic force microscopy (AFM, BRUKER, Dimension Icon). Nitrogen adsorption-desorption isotherms were collected by Autosorb-IQ-MP-C station).

Electrochemical measurements

The electrochemical tests were carried out on a CHI electrochemical workstation (CH Instrument Co. Shanghai) equipped with high-speed rotators from Pine Instruments. The typical three-electrode configuration was used with a Pt wire and a saturated Ag/AgCl electrode as the counter and reference electrode, respectively. To prepare the working electrode, 5 mg of catalysts were dispersed in the 1 mL of deionized water under sonication for 1 h to form a homogeneous ink. 15 μ L of the catalyst ink was loaded onto a mirror-polished glassy carbon electrode and dried at room temperature. Then the electrode was coated with 7.5 μ L of 0.1 wt% Nafion solution, and left to dry under ambient conditions before use.

The ORR and OER activity tests were determined from cyclic voltammetry at a scan rate of 5 mV s⁻¹ in O₂-saturated 0.1 M KOH aqueous solution unless otherwise stated. The potential was referenced respect to the reversible hydrogen electrode (RHE), which is obtained by adding a value of (0.196 + 0.059 pH) V to the potential measured against the Ag/AgCl electrode.

All the measurements were carried out at room temperature and the polarization data of the OER were iR-corrected.

For the ORR process, the transferred electron number (n) per oxygen molecule was determined from the slope of the Koutecky–Levich plot using the Koutecky–Levich equation,

$$\frac{1}{j} = \frac{1}{j_k} + \frac{1}{j_L} = \frac{1}{j_k} + \left(\frac{1}{0.2nFD_0^{2/3}v^{-1/6}C_0} \right) \omega^{-1/2}$$

where j is the measured current density, j_k is the kinetic current density, j_L is the diffusion-limiting current densities, F is the Faraday constant (96485 C mol⁻¹), D_0 is the diffusion coefficient (1.93×10⁻⁵ cm² s⁻¹) of O₂ in 0.1 M KOH electrolyte, v is the kinematic viscosity of the solution (0.01009 cm² s⁻¹), C_0 is the concentration (1.26×10⁻⁶ mol cm⁻³) of O₂ in the bulk solution and ω is the angular rotation rate. The constant 0.2 is adopted when the rotation speed is expressed in rpm.

For the RRDE measurements, the percentage of intermediate production (HO₂⁻%) and the electron transfer number (n) were determined by the following equations:

$$HO_2^-(\%) = 200 \frac{I_r/N}{I_d + I_r/N} \quad n = 4 \frac{I_d}{I_d + I_r/N}$$

where I_d is the disk current, I_r is the ring current, and the N is the current collection efficiency of the Pt ring, which is determined to be 0.37.

For the OER process, the Tafel slopes were obtained by fitting the linear portion of the Tafel plots ($\eta = a + b \log|j|$, where η is the overpotential, b is the Tafel slope, and j is the current density) derived from the corresponding polarization curves.

The primary Zn-air batteries were tested in 6 M KOH with a home-made electrochemical cell. A polished zinc plate, and a carbon cloth coated with the prepared catalyst ink (1 mg cm⁻²) were used as the anode and air cathode, respectively. For the rechargeable Zn-air batteries, we used a two-electrode configuration assembled into the cell with 0.2 M ZnCl₂ and 6 M KOH mixed solution as the electrolyte. CHI electrochemical workstation was used to carry out the cycling test. Each cycle period was set to be 10 min for discharge and 10 min for charge at a current density of 5 mA cm⁻².

Conflicts of interest

There are no conflicts to declare.

Acknowledgements

This work was supported by the National Natural Science Foundation of China (No. 21775016), the Fundamental Research Funds for the Central Universities (N160502001), and the National Natural Science Foundation of Liaoning (2015020175).

References

- 1 Y. Li and H. Dai, *Chem. Soc. Rev.*, 2014, **43**, 5257-5275.
- 2 L. Li and A. Manthiram, *Adv. Energy Mater.*, 2016, **6**, 1502054.

- 3 S. S. Shinde, C. H. Lee, A. Sami, D. H. Kim, S. U. Lee and J. H. Lee, *ACS Nano*, 2017, **11**, 347-357.
- 4 J. Zhang, Z. Zhao, Z. Xia and L. Dai, *Nat. Nanotechnol.*, 2015, **10**, 444-452.
- 5 G. Fu, X. Yan, Y. Chen, L. Xu, D. Sun, J.-M. Lee and Y. Tang, *Adv. Mater.*, DOI: 10.1002/adma.201704609, 1704609-n/a.
- 6 Y. Jiao, Y. Zheng, M. T. Jaroniec and S. Z. Qiao, *Chem. Soc. Rev.*, 2015, **44**, 2060-2086.
- 7 Z. W. Chen, D. Higgins, A. P. Yu, L. Zhang and J. J. Zhang, *Energy Environ. Sci.*, 2011, **4**, 3167-3192.
- 8 J. H. Wang, W. Cui, Q. Liu, Z. C. Xing, A. M. Asiri and X. P. Sun, *Adv. Mater.*, 2016, **28**, 215-230.
- 9 L. Han, S. J. Dong and E. K. Wang, *Adv. Mater.*, 2016, **28**, 9266-9291.
- 10 G. Wu and P. Zelenay, *Acc. Chem. Res.*, 2013, **46**, 1878-1889.
- 11 Y. Li, F. Cheng, J. Zhang, Z. Chen, Q. Xu and S. Guo, *Small*, 2016, **12**, 2839-2845.
- 12 Y. Y. Liang, Y. G. Li, H. L. Wang, J. G. Zhou, J. Wang, T. Regier and H. J. Dai, *Nat. Mater.*, 2011, **10**, 780-786.
- 13 A. L. Mohana Reddy, N. Rajalakshmi and S. Ramaprabhu, *Carbon*, 2008, **46**, 2-11.
- 14 Y. Liu, H. Cheng, M. Lyu, S. Fan, Q. Liu, W. Zhang, Y. Zhi, C. Wang, C. Xiao, S. Wei, B. Ye and Y. Xie, *J. Am. Chem. Soc.*, 2014, **136**, 15670-15675.
- 15 T. Y. Ma, S. Dai, M. Jaroniec and S. Z. Qiao, *J. Am. Chem. Soc.*, 2014, **136**, 13925-13931.
- 16 P. Chen, K. Xu, Z. Fang, Y. Tong, J. Wu, X. Lu, X. Peng, H. Ding, C. Wu and Y. Xie, *Angew. Chem.*, 2015, **54**, 14710-14714.
- 17 Y. R. Zheng, M. R. Gao, Q. Gao, H. H. Li, J. Xu, Z. Y. Wu and S. H. Yu, *Small*, 2015, **11**, 182-188.
- 18 M. Gong, W. Zhou, M.-C. Tsai, J. Zhou, M. Guan, M.-C. Lin, B. Zhang, Y. Hu, D.-Y. Wang, J. Yang, S. J. Pennycook, B.-J. Hwang and H. Dai, *Nat. Mater.*, 2014, **5**.
- 19 R. Cao, J.-S. Lee, M. Liu and J. Cho, *Adv. Energy Mater.*, 2012, **2**, 816-829.
- 20 G. Fu, Y. Chen, Z. Cui, Y. Li, W. Zhou, S. Xing, Y. Tang and J. B. Goodenough, *Nano Lett.*, 2016, **16**, 6516-6522.
- 21 G. Fu, Z. Cui, Y. Chen, L. Xu, Y. Tang and J. B. Goodenough, *Nano Energy*, 2017, **39**, 77-85.
- 22 R. Ma, Z. Liu, L. Li, N. Iyi and T. Sasaki, *J. Mater. Chem.*, 2006, **16**, 3809-3813.
- 23 G. Fan, F. Li, D. G. Evans and X. Duan, *Chem. Soc. Rev.*, 2014, **43**, 7040-7066.
- 24 L. Li, W. Gu, J. Chen, W. Chen and Z. P. Xu, *Biomaterials*, 2014, **35**, 3331-3339.
- 25 S. Cho, J.-W. Jang, Y. B. Park, J. Y. Kim, G. Magesh, J. H. Kim, M. Seol, K. Yong, K.-H. Lee and J. S. Lee, *Energy Environ. Sci.*, 2014, **7**, 2301-2307.
- 26 M. Shao, M. Wei, D. G. Evans and X. Duan, *Chemical Communications*, 2011, **47**, 3171-3173.
- 27 X. Long, J. Li, S. Xiao, K. Yan, Z. Wang, H. Chen and S. Yang, *Angew. Chem., Int. Ed.*, 2014, **53**, 7584-7588.
- 28 M. Gong, Y. Li, H. Wang, Y. Liang, J. Z. Wu, J. Zhou, J. Wang, T. Regier, F. Wei and H. Dai, *J. Am. Chem. Soc.*, 2013, **135**, 8452-8455.
- 29 H.-F. Wang, C. Tang, B. Wang, B.-Q. Li and Q. Zhang, *Adv. Mater.*, 2017, **29**, 1702327.
- 30 Q. Wang, L. Shang, R. Shi, X. Zhang, Y. Zhao, G. I. N. Waterhouse, L.-Z. Wu, C.-H. Tung and T. Zhang, *Adv. Energy Mater.*, 2017, **7**, 1700467.
- 31 K. L. Chee, N. A. Mohd Zabidi and C. Mohan, *Defect Diffus. Forum*, 2011, **312-315**, 370-375.
- 32 J. C. Sánchez-López, T. C. Rojas, J. P. Espinós and A. Fernández, *Scr. Mater.*, 2001, **44**, 2331-2334.
- 33 W. Xia, R. Zou, L. An, D. Xia and S. Guo, *Energy Environ. Sci.*, 2015, **8**, 568-576.
- 34 H.-F. Wang, C. Tang, X. Zhu and Q. Zhang, *J. Mater. Chem. A*, 2016, **4**, 3379-3385.

ARTICLE

Journal Name

- 35 Y. Su, Y. Zhu, H. Jiang, J. Shen, X. Yang, W. Zou, J. Chen and C. Li, *Nanoscale*, 2014, **6**, 15080-15089.
- 36 D. U. Lee, B. J. Kim and Z. Chen, *J. Mater. Chem. A*, 2013, **1**, 4754.
- 37 H. Cheng, M.-L. Li, C.-Y. Su, N. Li and Z.-Q. Liu, *Adv. Funct. Mater.*, 2017, **27**, 1701833.
- 38 S. Mao, Z. Wen, T. Huang, Y. Hou and J. Chen, *Energy Environ. Sci.*, 2014, **7**, 609-616.
- 39 G. Fu, Z. Cui, Y. Chen, Y. Li, Y. Tang and J. B. Goodenough, *Adv. Energy Mater.*, 2017, **7**, 1601172.
- 40 J. Parrondo, T. Han, E. Niangar, C. Wang, N. Dale, K. Adjemian and V. Ramani, *Proc. Natl. Acad. Sci. U. S. A.*, 2014, **111**, 45-50.
- 41 Y.-J. Wang, D. P. Wilkinson and J. Zhang, *Chem. Rev.*, 2011, **111**, 7625-7651.
- 42 M. Bajdich, M. Garcia-Mota, A. Vojvodic, J. K. Nørskov and A. T. Bell, *J. Am. Chem. Soc.*, 2013, **135**, 13521-13530.
- 43 B. S. Yeo and A. T. Bell, *J. Am. Chem. Soc.*, 2011, **133**, 5587-5593.
- 44 M. R. Gao, Y. F. Xu, J. Jiang, Y. R. Zheng and S. H. Yu, *J. Am. Chem. Soc.*, 2012, **134**, 2930-2933.
- 45 X. Liu, M. Park, M. G. Kim, S. Gupta, G. Wu and J. Cho, *Angew. Chem.*, 2015, **54**, 9654-9658.
- 46 X. Liu, M. Park, M. G. Kim, S. Gupta, X. Wang, G. Wu and J. Cho, *Nano Energy*, 2016, **20**, 315-325.
- 47 Y. Li, M. Gong, Y. Liang, J. Feng, J. E. Kim, H. Wang, G. Hong, B. Zhang and H. Dai, *Nat. Commun.*, 2013, **4**, 1805.
- 48 M. Li, Y.-X. Yin, C. Li, F. Zhang, L.-J. Wan, S. Xu and D. G. Evans, *Chem. Commun.*, 2012, **48**, 410-412.